nature physics

LETTERS

https://doi.org/10.1038/s41567-019-0427-6

Dimensional reduction, quantum Hall effect and layer parity in graphite films

Jun Yin[1,2], Sergey Slizovskiy[1,2], Yang Cao[1,3,4], Sheng Hu[1,3], Yaping Yang[1,2], Inna Lobanova[5], Benjamin A. Piot[5], Seok-Kyun Son[1,2], Servet Ozdemir[1,2], Takashi Taniguchi[6], Kenji Watanabe[6], Kostya S. Novoselov[1,2], Francisco Guinea[7,2], A. K. Geim[1,2*], Vladimir Fal'ko[1,2,8*] and Artem Mishchenko[1,2*]

The quantum Hall effect (QHE) originates from discrete Landau levels forming in a two-dimensional electron system in a magnetic field[1]. In three dimensions, the QHE is forbidden because the third dimension spreads Landau levels into overlapping bands, destroying the quantization. Here we report the QHE in graphite crystals that are up to hundreds of atomic layers thick, a thickness at which graphite was believed to behave as a normal, bulk semimetal[2]. We attribute this observation to a dimensional reduction of electron dynamics in high magnetic fields, such that the electron spectrum remains continuous only in the field direction, and only the last two quasi-one-dimensional Landau bands cross the Fermi level[3,4]. Under these conditions, the formation of standing waves in sufficiently thin graphite films leads to a discrete spectrum allowing the QHE. Despite the large thickness, we observe differences between crystals with even and odd numbers of graphene layers. Films with odd layer numbers show reduced QHE gaps, as compared to films of similar thicknesses but with even numbers because the latter retain the inversion symmetry characteristic of bilayer graphene[5,6]. We also observe clear signatures of electron–electron interactions including the fractional QHE below 0.5 K.

The Lorentz force imposed by a magnetic field, B, changes the straight ballistic motion of electrons into spiral trajectories aligned along B (Fig. 1a). This spiral motion gives rise to Landau bands that are characterized by plane waves propagating along the B direction but quantized in the directions perpendicular to the magnetic field[7]. The increase in B changes the distance between Landau bands, and the resulting crossings of the Fermi level, E_F, with the Landau band edges lead to quantum oscillations. When only the lowest few Landau bands cross E_F (ultra-quantum regime (UQR)), the magnetic field effectively makes the electron motion one-dimensional (1D) (with conductivity allowed only in the direction parallel to B). In normal metals such as copper, this dimensional reduction would require $B > 10{,}000$ T. In semimetals with their small Fermi surfaces (graphite[2,4,8], for example), the dimensional reduction and the UQR can be reached in moderate B. Indeed, magnetotransport measurements in bulk crystals[4,9–11] and films of graphite[12,13] revealed quantum oscillations reaching the lowest Landau bands. However, no dissipationless QHE transport could be observed as expected for the 3D systems.

The UQR in graphite can be reached when $B > 7$ T (ref. [4]) where all electrons near the Fermi level belong to the two half-filled 1D bands emerging from the lowest (0 and 1) Landau levels of bilayer graphene that is the building block of Bernal-stacked graphite[5]. At the opposite edges of the 3D Brillouin zone (lines +KH and −KH, designated below as valleys) these 0 and 1 states reside on alternating atomic planes of carbon atoms, and in the bulk graphite crystal the inversion symmetry of its bilayer unit cell makes these spectra valley-degenerate. The 1D character of Landau bands in graphite in the UQR suggests the formation of charge-density-wave states[14] at $B > 25$ T due to their half-filling and of an insulating phase[15] at even higher $B > 70$ T, where the splitting between the 0 and 1 Landau bands exceeds their bandwidth. In our case of thin graphite crystals, these quasi-1D bands split into a set of standing waves separated by $\Delta k_z = \pi/L$, where L is the crystal thickness (Fig. 1a). The standing waves lead to discretization of the electronic spectrum and, therefore, can in principle allow the QHE that is otherwise forbidden in three dimensions. Here we show that, in the UQR, high-quality graphite films of a submicrometre thickness indeed exhibit the fully developed QHE with quantized Hall and zero longitudinal resistances. Moreover, the standing waves retain the valley-layer correspondence of the 0 and 1 bulk Landau bands so that crystals with an even number of layers N retain the valley degeneracy in the standing-wave spectrum whereas the degeneracy is lifted for odd N because of the lack of inversion symmetry[6]. In a way, the described films exhibit the electronic properties of both 3D and 2D conductors and, hence, can be referred to as a 2.5D system.

To prepare our devices, we cleaved natural graphite crystals along their basal planes using the micromechanical exfoliation technique[16]. Then we encapsulated the cleaved crystals in hexagonal boron nitride (hBN), expanding the technology of van der Waals heterostructures to 3D systems[17]. Due to a self-cleansing mechanism, this approach results in quality atomically flat interfaces with little electron scattering at the surfaces[18,19]. We focus on crystals with thicknesses above 10 graphene layers ($L > 3.5$ nm), which are commonly considered as 3D graphite electronically[20]. For the upper limit of L, we chose thicknesses of about 100 nm because

[1]National Graphene Institute, University of Manchester, Manchester, UK. [2]School of Physics and Astronomy, University of Manchester, Manchester, UK. [3]College of Chemistry and Chemical Engineering, Collaborative Innovation Center of Chemistry for Energy Materials, Xiamen University, Xiamen, China. [4]State Key Laboratory of Physical Chemistry of Solid Surface, Xiamen University, Xiamen, China. [5]Laboratoire National des Champs Magnétiques Intenses, LNCMI-CNRS-UGA-UPS-INSA-EMFL, Grenoble, France. [6]National Institute for Materials Science, Tsukuba, Japan. [7]IMDEA Nanoscience, Madrid, Spain. [8]Henry Royce Institute for Advanced Materials, Manchester, UK. *e-mail: geim@manchester.ac.uk; vladimir.falko@manchester.ac.uk; artem.mishchenko@gmail.com

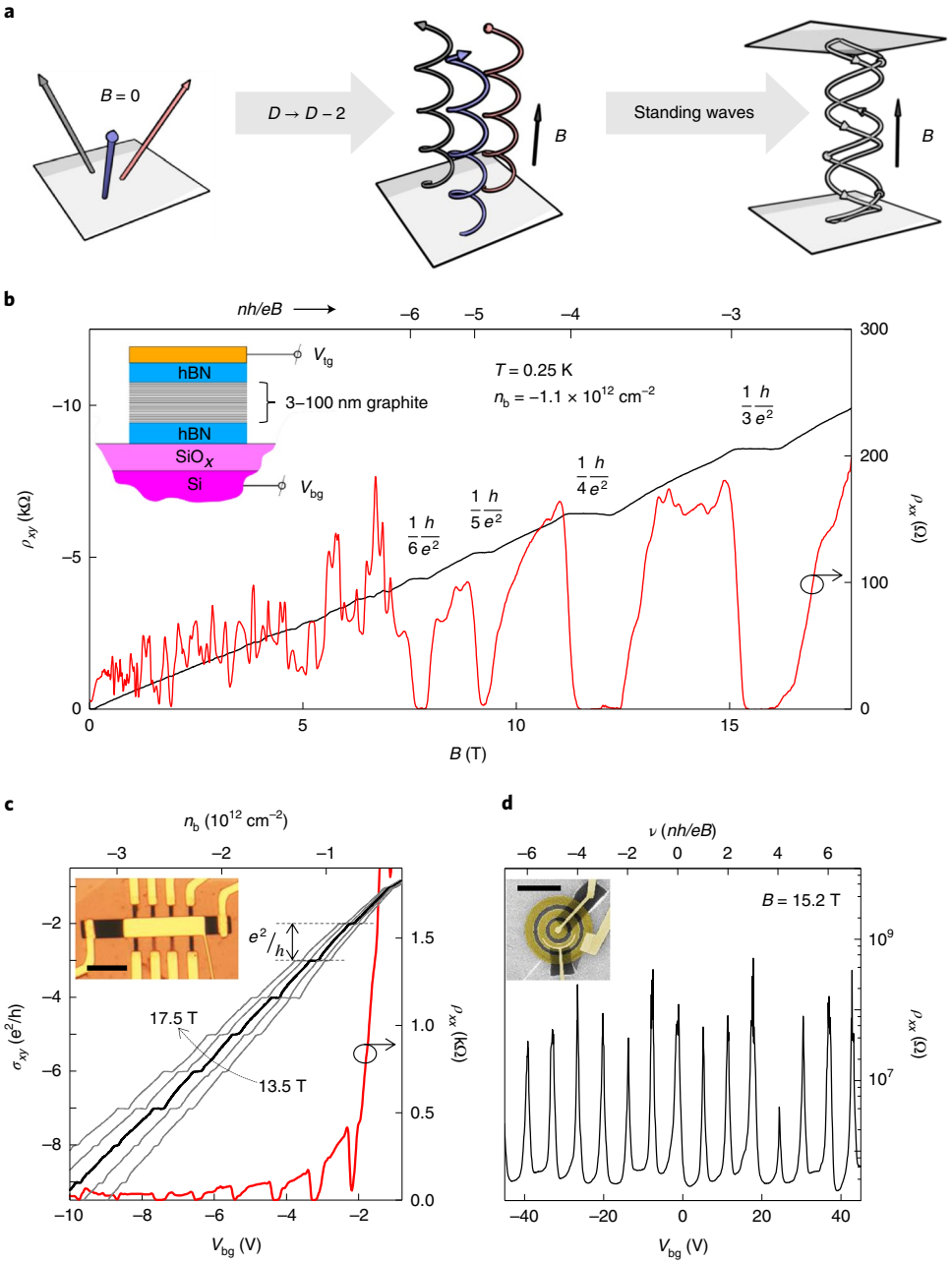

Fig. 1 | QHE in 3D graphite. a, Ballistic electron trajectories in the absence of magnetic field (left schematic) undergo dimensional reduction into cyclotron spirals in high fields (middle). In thin crystals, the spiral trajectories can form standing waves (right). **b**, Transversal ρ_{xy} (black curve) and longitudinal ρ_{xx} (red) resistivity as a function of B, measured at 0.25 K in a 6-nm-thick graphite device. The density $n_b = -1.1 \times 10^{12}$ cm^{-2} is induced by applying a back-gate voltage and the negative sign corresponds to holes. The inset shows a schematic of our hBN/graphite/hBN heterostructures. **c**, Hall conductivity σ_{xy} (black curve) and ρ_{xx} (red) as a function of back-gate voltage V_{bg} at $B = 15.5$ T. Grey curves: measurements at B from 13.5 to 17.5 T; $T = 0.25$ K; $V_{tg} = 0$ V; same device as in **b**. Inset: optical micrograph of the used Hall bar device (scale bar, 10 μm). **d**, ρ_{xx} in the Corbino geometry; $T = 0.25$ K; $L = 10$ nm. ρ_{xx} diverges at the integer filling factors ν (top x axis). Inset: false-colour scanning electron micrograph of the Corbino device. Scale bar, 5 μm.

an average distance between stacking faults in natural graphite is known to be 100–200 nm[21,22] and those defects efficiently decouple electronic states in different parts of graphene stacks[23]. All of our devices showed a metallic temperature dependence of resistivity (see, for example, Supplementary Fig. 1). Above 30 K the mobility of charge carriers followed a $1/T$ dependence, in agreement with the earlier studies[24,25], and saturated below 10 K to approximately 4×10^5 cm^2 V^{-1} s^{-1}.

As we turned the magnetic field on, our devices exhibited strong positive magnetoresistance such that the longitudinal resistivity ρ_{xx} notably increased with increasing B from 0 to 0.4 T (Supplementary Fig. 1), which is typical for compensated semimetals[26]. Already at fairly low B below 0.1 T, we observed clear Shubnikov–de Haas oscillations that developed into the QHE above approximately 7 T (Fig. 1b). Indeed, one can see that around $B = nh/e\nu$, the Hall resistivity ρ_{xy} plateaus out at unit fractions of h/e^2, which is accompanied by vanishing ρ_{xx}. Here, n is the electrostatically controlled carrier density, h is the Planck constant, e is the elementary charge and ν is the Landau filling factor that relates n to the flux quantum, h/e. The QHE is also clearly seen if we fixed B and changed n (Fig. 1c).

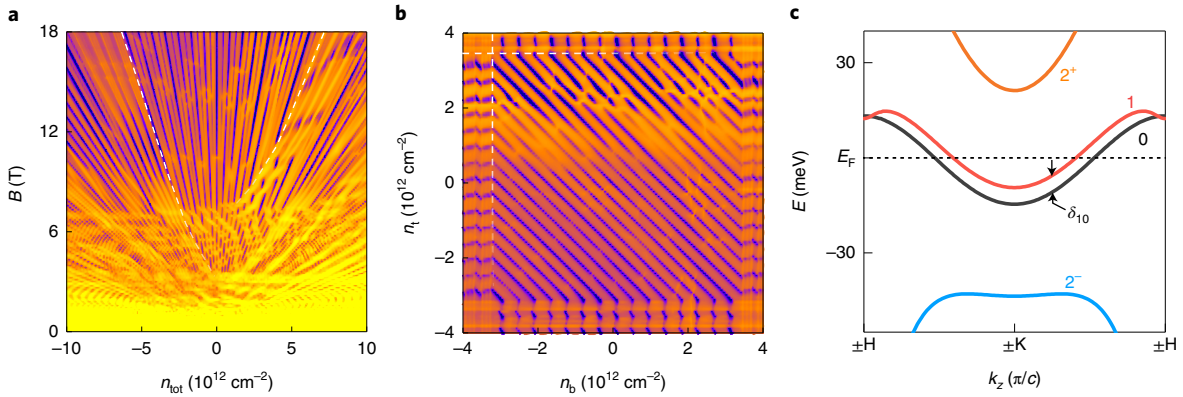

Fig. 2 | Landau levels in thin graphite films. a, σ_{xx} as a function of B and n_{tot} measured at $n_t = n_b$ in a Corbino device with $L = 11.6$ nm; $T = 0.25$ K. The white dashed curves are guides to the eye for the features arising from the Landau quantization of electrostatically induced surface states. **b**, Map of σ_{xx} (n_t, n_b) at 18 T. The horizontal and vertical features at the edges of the map (shown by white contour lines) are due to the quantized states at the graphite surfaces. The diagonal features are ascribed to the k_z-quantized lowest Landau bands that extend through the graphite bulk (2.5D QHE). Logarithmic colour scales for both **a** and **b**; navy to yellow is 50 nS to 50 μS. **c**, Dispersion relation for low Landau bands calculated using the tight-binding model at 15 T (Methods). Only the lowest two bands (labelled as 0 and 1, and split by δ_{10}) cross the Fermi level.

Note that current densities as low as 50 nA μm^{-1} were sufficient to suppress the QHE (Supplementary Fig. 2). Vanishing ρ_{xx} (and σ_{xx}) signifies dissipationless transport along the edges of the otherwise insulating films[1]. We confirmed these insulating states using the edgeless (Corbino) geometry: Fig. 1d shows the insulating behaviour of a 10-nm-thick Corbino device where, for integer ν, ρ_{xx} exceeds 0.1 GΩ.

In graphite, mobile charge carriers induced by gate voltages are mainly localized in the first couple of layers near the surface because of electrostatic screening. Since the 0 and 1 Landau bands cross E_F at almost half-filling (Fig. 2c), their surface states coexist and mix with the bulk states, making the two graphite surfaces interconnected (correlated). However, for sufficiently high doping the situation is expected to change because higher Landau bands can also become occupied, which results in charge accumulation near the surfaces. The resulting surface states decay exponentially into the bulk, and this breaks down correlations between the two surfaces. To disentangle the contributions from the bulk and surface states to the observed QHE we carried out transport measurements in a double-gated Corbino device (Fig. 2) and electronic compressibility measurements in a double-gated capacitor device (Supplementary Fig. 3). With the two gates, we can induce charge carriers at the top (n_t) and bottom (n_b) surfaces independently. Longitudinal conductivity $\sigma_{xx}(B)$ as a function of the electrostatically induced density $n_{tot} = n_t + n_b$ is shown by a colour map in Fig. 2a where metallic states (bright colours) fan out from the neutrality point, $n_{tot} = 0$. The majority of the observed features can be attributed to the discussed 2.5D QHE states as in high fields they are linear in B, and their slopes B/n_{tot} follow integer filling factors. However, there is a notable change at approximately 7 T, below which the QHE is obscured by a complicated criss-crossing behaviour (the existence of the critical field manifests itself even more clearly in thicker devices, see Supplementary Fig. 4). In addition, we also observe features that are not linear in B and do not follow the integer ν, examples of which are indicated by the dashed curves in Fig. 2a. We attribute those quantized levels to the 2D accumulation layers at the two graphite surfaces (for discussion, see Methods). The difference between the quantized features due to the surface states and those due to the 2.5D QHE is especially obvious from the maps of σ_{xx} (n_t, n_b) at a fixed B (Fig. 2b; also, Supplementary Fig. 3). The 2.5D QHE states formed by the standing waves in the bulk follow the diagonal lines on the map; that is, both top and bottom gates contribute equally to the filling of the Landau states that penetrate through the whole bulk. In contrast, the quantized states at the top and bottom surfaces follow horizontal and vertical lines, respectively, which indicates that the states are electronically decoupled and interactions between the two surfaces are screened out[27]. To better understand the origin of the surface states we performed self-consistent tight-binding/Hartree calculations (Methods), and the computed density of states and carrier density profiles are presented in Supplementary Fig. 3.

The conductivity maps in Fig. 2 also show that the gaps along the integer filling factors can close and reopen as a function of both n and B, which is indicative of level crossings. To explain the observed patterns, we refer to the band structure of graphite in the Slonczewski–Weiss–McClure (SWMC) tight-binding model[2,8,28,29] for Bernal-stacked graphite (see Methods). At zero field, the low-energy electronic structure is dominated by two bands in two valleys[2,8,28] that are degenerate for $k_{x,y} = \pm$K and weakly disperse in k_z (+KH and −KH valleys). In quantizing fields[4,29], these are reduced to two nearly coinciding Landau bands 0 and 1 (Fig. 2c). They cross the Fermi level close to $k_F \approx \pi/4c$ ($c = 0.335$ nm is the interlayer distance in graphite), exhibit the 1D Fermi velocity $v_F \approx 15{,}000$ m s^{-1} and are split by $\delta_{10} \approx 0.37$ meV T^{-1} (Methods).

In graphite crystals with a small L, electrons in the two Landau bands 0 and 1 form standing waves, which for different valleys reside on graphene layers of opposite parity: the states in the +KH valley live on the even layers, and the states in the −KH valley on the odd ones (see Methods). For even-N crystals, there is the same number of even and odd layers to support states in both +KH and −KH valleys, leading to the valley-degenerate ladder of states that are spaced in k_z by the distance $\frac{\pi}{c(N+2)}$. In odd-N crystals, the number of even and odd states differs by one, which results in a k_z-shift of approximately $\frac{\pi}{2c(N+1)}$ between the two ladders, around the Fermi level. This shift lifts the valley degeneracy and, therefore, reduces the energy spacing, δE_{odd}, by nearly a factor of two as compared to the even-N films (see Fig. 3a). We refer to this difference between the standing-wave spectra in graphite with even and odd N as the layer-parity effect.

To test this effect, we measured the 2.5D QHE in several pairs of Corbino devices, in which the thickness differed only by a single graphene layer. We fabricated these pairs from the same graphite crystals having monatomic steps on the surface (Methods). The transport measurements were performed in sufficiently high B to induce spin polarization; that is, $2\mu_B B > k_B T$, where μ_B is the Bohr

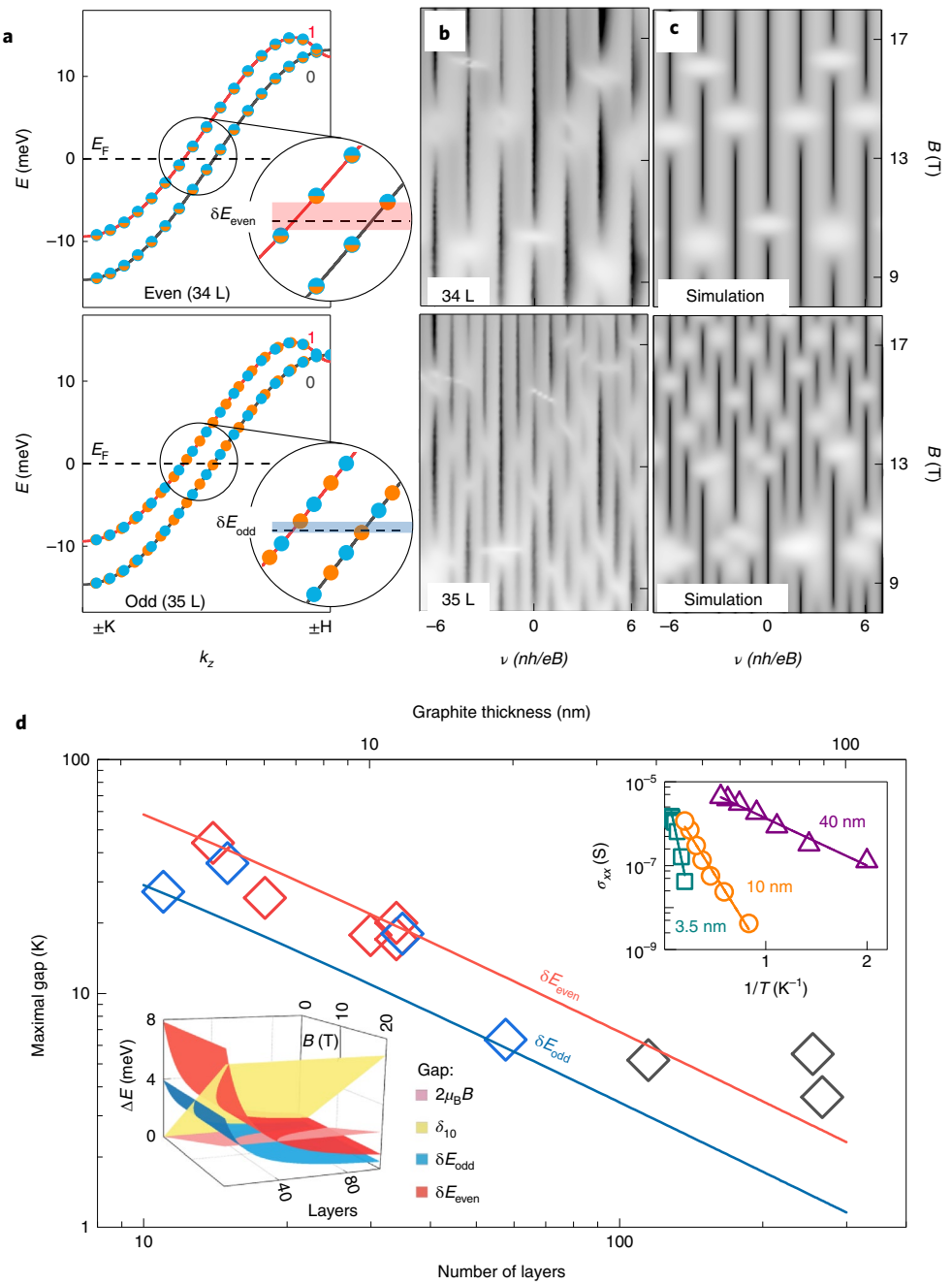

Fig. 3 | Thickness and layer-parity dependence of the 2.5D QHE. a, $E(k_z)$ for the two lowest Landau bands in graphite (grey and red curves). The blue and orange dots are the standing-wave states caused by k_z-quantization calculated for +KH and −KH valleys, respectively. The top and bottom panels are for even $N=34$ and odd $N=35$, respectively. **b**, $\sigma_{xx}(B, \nu)$ for 34- and 35-layer devices (top and bottom panels, respectively) measured at 1 K. Logarithmic greyscale: black to white is 0.1 to 5.6 μS. Note the double degeneracy ($\Delta\nu=2$) for even-layered graphite and the fully lifted degeneracy ($\Delta\nu=1$) for the odd-layered one. **c**, Calculated density of states as a function of B and ν for the graphite device in **b**. Logarithmic scale: black to white is 0.01 to 1.5 eV^{-1}nm^{-2} and 0.01 to 1 eV^{-1}nm^{-2} for the top and bottom panels, respectively. **d**, Energy gaps for the 2.5D QHE as a function of thickness. Shown are the maximal gaps found away from level crossings. Red symbols, graphite devices with even N; blue symbols, odd N; black symbols, unconfirmed parity. The red and blue lines are the gaps estimated from the free-particle model. Top inset: examples of Arrhenius plots for three devices. Bottom inset: relative strengths of $\delta E_{even/odd}$, δ_{10} and $2\mu_B B$ (Zeeman splitting) gaps as a function of N and B.

magneton and k_B is the Boltzmann constant. Figure 3b shows that for the 34-layer graphite device the degeneracy of the QHE states was 2 whereas all of the unit steps in ν were observed for the device with $N=35$. This indicates that all of the degeneracies were lifted in the latter case, including the valley degeneracy. Data for devices with $N=14$ and 15 are presented in Supplementary Fig. 5.

The pronounced level crossings seen in the maps of Figs. 2 and 3 can also be related to specifics of the 2.5D QHE in graphite. This behaviour arises due to competition between the Landau band splitting, δ_{10}, the spin splitting, $2\mu_B B$, and the B-independent standing wave spacing, $\delta E_{even/odd}$, which all lead to a complex hierarchy of energy gaps and numerous level crossings with changing B. The

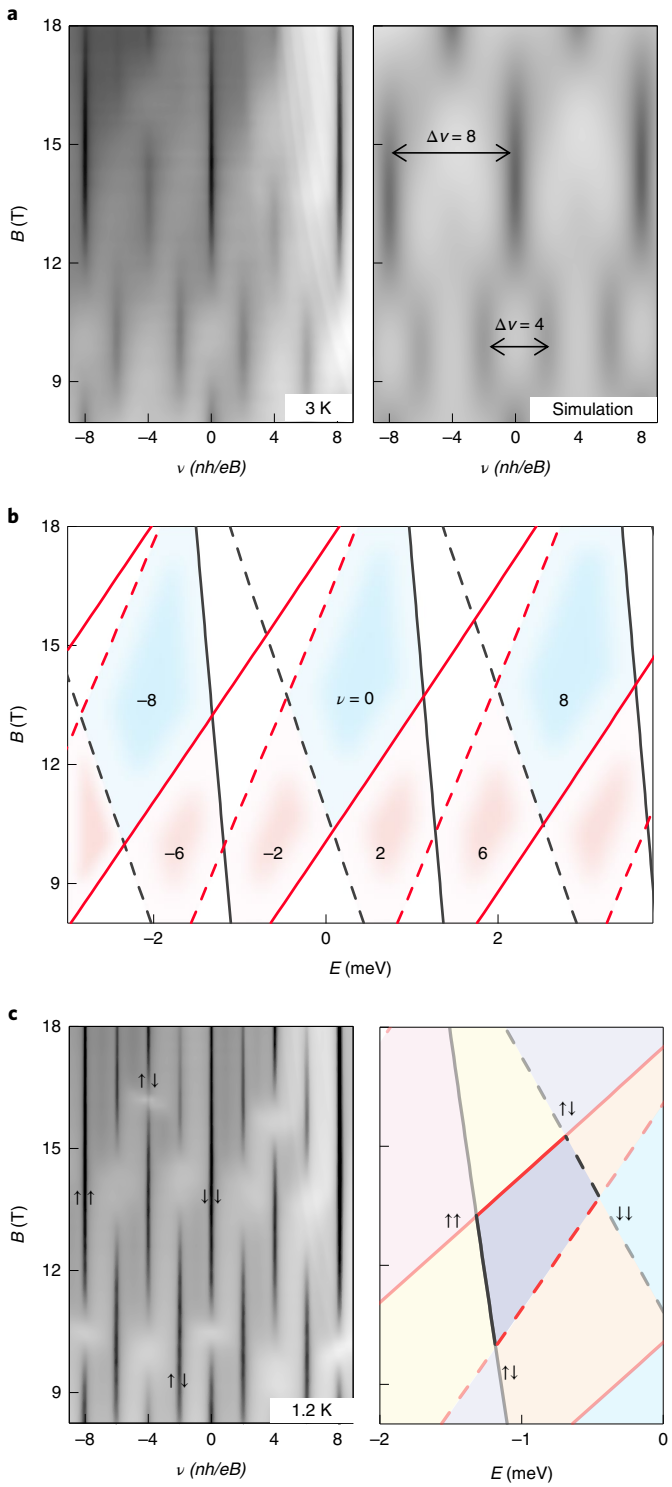

Fig. 4 | Hierarchy of QHE gaps and level crossings in the UQR. a, Left panel: map of σ_{xx} (B,ν) for the device in Fig. 2; $T = 3$ K. Logarithmic grey scale: black to white is 0.6 to 5.6 μS. Right panel: calculated density of states as a function of B and ν. Colour scale: black to white is 0.1 to 2 $eV^{-1}nm^{-2}$. **b**, Calculated 0 (black) and 1 (red) Landau bands of 34-layer graphite. The solid (dashed) lines are ↑ (↓) spin states. The Landau level crossings result in QHE-gap closures in **a**. **c**, Left panel: the same as in the left panel of **a** but the measurements were performed at 1.2 K. Logarithmic scale: black to white is 0.1 to 7.4 μS. Right panel: zoomed-in region of **b**. Gap closures in the left panel of **c** and the level crossings in the right panel of **c** are labelled by the corresponding spin states ↑ and ↓. The coloured background specifies $\nu = -8$ (pink), −6 (yellow), −4 (violet), −2 (orange) and 0 (blue).

bottom inset in Fig. 3d summarizes the expected interplay between the gap sizes for different fields, thicknesses and parities (Methods and Supplementary Fig. 6). Figure 3 also shows the measured maximal QHE gaps, ΔE, for each of the studied samples with different L. The gaps were measured away from level crossings using the Arrhenius model for the dissipative conductivity in the QHE regime, $\sigma_{xx} \propto e^{-\Delta E/2k_BT}$ (top inset of Fig. 3d). The red and blue curves show the upper bounds for ΔE as found in our modelling for even and odd N, respectively.

We show more details of the level crossing behaviour in Fig. 4. Figure 4a compares the measured and simulated σ_{xx} (B, ν) for the 11.6 nm device in Fig. 2. In both cases there are two periods, $\Delta\nu$, at which crossings occur: $\Delta\nu = 4$ and 8. For $N > 20$, we estimate (see Methods) that $\delta E_{even/odd} < \delta_{10}$ for the experimental range of B and, therefore, the level crossings are dominated by fast changes in the Landau band splitting. Figure 4b highlights the complex hierarchy of gaps for different B. For example, at about 13 T, 4 valley-degenerate levels approach each other, which effectively results in relatively large gaps between crossings and, therefore, in robust quantization such that steps with $\Delta\nu = 8$ persist to $k_BT \approx \delta E_{even} \approx 94N^{-1}$ meV (this dependence is also shown by the red curve in Fig. 3d). On the other hand, at around 10 T, valley-degenerate levels cross at some distance from each other, resulting in approximately twice smaller gaps and steps with $\Delta\nu = 4$, as observed in both experiment and simulations. Similarly, for films with odd N, in which the valley degeneracy is lifted, the upper limit for the 2.5D QHE gaps is set by $\delta E_{odd} \approx 47N^{-1}$ meV (blue curve in Fig. 3d). Note that the observed dependences $\delta E(N)$ imply that, at millikelvin temperatures, the 2.5D QHE should be observable even in micrometre-thick graphite, if no stacking faults are present that would probably suppress the quantization.

The free-particle (non-interacting) model describes all of the main characteristics of the observed QHE confirming that the phenomenon arises due to the standing waves and is controlled mostly by graphite's thickness and layer parity. However, at our highest B and lowest T, the devices also exhibit features indicating that electron–electron interactions contribute to the electronic properties. For example, Fig. 4c and Supplementary Fig. 7a show that crossings between the same-spin states are much broader than those between the opposite-spin states, which suggests some magnetic ordering[30]. Besides, even-layer graphite devices exhibit spontaneous valley polarization at $T < 0.5$ K (Supplementary Fig. 7f–g). For relatively thin devices ($L = 3$–4 nm) we also observed the onset of the fractional QHE (Supplementary Fig. 8). The general expectation is that electron–electron interactions can trigger a variety of phase transitions in the form of density waves, excitonic condensation or Wigner crystals[15,31,32], and the high-quality graphite films introduced in this work offer a venue (especially, at millikelvin temperatures) to study such transitions with many competing order parameters.

Online content

Any methods, additional references, Nature Research reporting summaries, source data, statements of data availability and associated accession codes are available at https://doi.org/10.1038/s41567-019-0427-6.

Received: 23 December 2018; Accepted: 14 January 2019;
Published online: 25 February 2019

References

1. Yoshioka, D. *The Quantum Hall Effect* (Springer, Berlin, 1998).
2. McClure, J. W. Band structure of graphite and de Haas–van Alphen effect. *Phys. Rev.* **108**, 612–618 (1957).
3. Shovkovy, I. A. Magnetic catalysis: a review. *Lecture Notes Phys.* **871**, 13–49 (2013).
4. McClure, J. W. & Spry, W. J. Linear magnetoresistance in the quantum limit in graphite. *Phys. Rev.* **165**, 809–815 (1968).

5. McCann, E. & Fal'ko, V. I. Landau-level degeneracy and quantum Hall effect in a graphite bilayer. *Phys. Rev. Lett.* **96**, 086805 (2006).
6. Koshino, M. & McCann, E. Landau level spectra and the quantum Hall effect of multilayer graphene. *Phys. Rev. B* **83**, 165443 (2011).
7. Landau, L. D. & Lifshitz, E. M. *Quantum Mechanics* 3rd edn (Pergamon, Oxford, 1977).
8. Slonczewski, J. C. & Weiss, P. R. Band structure of graphite. *Phys. Rev.* **109**, 272–279 (1958).
9. Brandt, N. B., Kapustin, G. A., Karavaev, V. G., Kotosonov, A. S. & Svistova, E. A. Investigation of galvanomagnetic properties of graphite in magnetic-fields up to 500 kOe at low temperatures. *Zh. Eksp. Teor. Fiz.* **40**, 564–569 (1974).
10. Kopelevich, Y. et al. Reentrant metallic behavior of graphite in the quantum limit. *Phys. Rev. Lett.* **90**, 156402 (2003).
11. Luk'yanchuk, I. A. & Kopelevich, Y. Phase analysis of quantum oscillations in graphite. *Phys. Rev. Lett.* **93**, 166402 (2004).
12. Morozov, S. V. et al. Two-dimensional electron and hole gases at the surface of graphite. *Phys. Rev. B* **72**, 201401 (2005).
13. Zhang, Y. B., Small, J. P., Pontius, W. V. & Kim, P. Fabrication and electric-field-dependent transport measurements of mesoscopic graphite devices. *Appl. Phys. Lett.* **86**, 073104 (2005).
14. Zhu, Z. et al. Magnetic field tuning of an excitonic insulator between the weak and strong coupling regimes in quantum limit graphite. *Sci. Rep.* **7**, 1733 (2017).
15. Arnold, F. et al. Charge density waves in graphite: towards the magnetic ultraquantum limit. *Phys. Rev. Lett.* **119**, 136601 (2017).
16. Novoselov, K. S. et al. Electric field effect in atomically thin carbon films. *Science* **306**, 666–669 (2004).
17. Wang, L. et al. One-dimensional electrical contact to a two-dimensional material. *Science* **342**, 614–617 (2013).
18. Geim, A. K. & Grigorieva, I. V. Van der Waals heterostructures. *Nature* **499**, 419–425 (2013).
19. Novoselov, K. S., Mishchenko, A., Carvalho, A. & Castro Neto, A. H. 2D materials and van der Waals heterostructures. *Science* **353**, aac9439 (2016).
20. Partoens, B. & Peeters, F. M. From graphene to graphite: electronic structure around the K point. *Phys. Rev. B* **74**, 075404 (2006).
21. Spain, I. L., Ubbelohde, A. R. & Young, D. A. Electronic properties of well oriented graphite. *Phil. Trans. R. Soc. A* **262**, 345–386 (1967).
22. Hedley, J. A. & Ashworth, D. R. Imperfections in natural graphite. *J. Nucl. Mater.* **4**, 70–78 (1961).
23. Arovas, D. P. & Guinea, F. Stacking faults, bound states, and quantum Hall plateaus in crystalline graphite. *Phys. Rev. B* **78**, 245416 (2008).
24. Soule, D. E. Magnetic field dependence of the Hall effect and magnetoresistance in graphite single crystals. *Phys. Rev.* **112**, 698–707 (1958).
25. Ono, S. & Sugihara, K. Theory of the transport properties in graphite. *J. Phys. Soc. Jpn* **21**, 861–868 (1966).
26. Brandt, N. B., Chudinov, S. M. & Ponomarev, Y. G. *Semimetals: 1. Graphite and its Compounds* (North-Holland, Amsterdam, 1988).
27. Guinea, F. Charge distribution and screening in layered graphene systems. *Phys. Rev. B* **75**, 235433 (2007).
28. Mikitik, G. P. & Sharlai, Y. V. Band-contact lines in the electron energy spectrum of graphite. *Phys. Rev. B* **73**, 235112 (2006).
29. McClure, J. W. Theory of diamagnetism of graphite. *Phys. Rev.* **119**, 606–613 (1960).
30. De Poortere, E. P., Tutuc, E., Papadakis, S. J. & Shayegan, M. Resistance spikes at transitions between quantum Hall ferromagnets. *Science* **290**, 1546–1549 (2000).
31. Halperin, B. I. Possible states for a three-dimensional electron gas in a strong magnetic field. *Jpn. J. Appl. Phys.* **26**, 1913 (1987).
32. Yoshioka, D. & Fukuyama, H. Electronic phase-transition of graphite in a strong magnetic-field. *J. Phys. Soc. Jpn* **50**, 725–726 (1981).

Acknowledgements

This work was supported by the EU Graphene Flagship Program, the European Research Council, the Royal Society and the Engineering and Physical Sciences Research Council. J.Y. and A.M. acknowledges the support of EPSRC Early Career Fellowship EP/N007131/1.

Author contributions

A.M., A.K.G. and J.Y. conceived the experiments. J.Y., I.L., S.O. and B.P. conducted the transport measurements. J.Y., Y.C., S.H., Y.Y. and S.-K.S. prepared the samples. A.M. and J.Y. performed data analysis. S.S. and V.F. developed theory and S.S., V.F. and F.G. interpreted the data and performed the tight-binding simulations. T.T. and K.W. provided hBN crystals. A.M. wrote the manuscript with input from V.F., A.K.G., J.Y., S.S., K.S.N and F.G.

Competing interests

The authors declare no competing interests.

Additional information

Supplementary information is available for this paper at https://doi.org/10.1038/s41567-019-0427-6.

Correspondence and requests for materials should be addressed to A.K.G., V.F. or A.M.

Methods

Device fabrication. Our hBN/graphite/hBN heterostructures were assembled using the dry transfer technology[17,33]. Graphite and hBN flakes were first mechanically exfoliated onto oxidized Si wafers. Then the top hBN and graphite crystals were sequentially picked up by a polymer bilayer of polydimethylsiloxane and polymethylmethacrylate (PMMA). The hBN/graphite stack was released onto the bottom hBN crystal, which completed the heterostructure. It is known that accurate crystallographic alignment between graphite and hBN crystal lattices can result in superlattice effects and, therefore, we intentionally misaligned the graphite with respect to both hBN crystals by angles larger than 5°. This makes the moiré period small and shifts the band structure reconstruction to energies inaccessible in transport measurements. Raman spectroscopy was also employed to confirm that the chosen graphite crystals had the Bernal (ABA) stacking[34] (Supplementary Fig. 9).

Electrical contacts to graphite were prepared by electron-beam lithography, which created openings in a PMMA resist and allowed us to remove the top hBN layer using reactive ion etching. Electron-beam evaporation was then used to deposit metal contacts Cr/Au (3 nm/80 nm) into the etched areas. Another round of electron-beam lithography and electron-beam evaporation was implemented to define the top gate, which also served as an etch mask to define the Hall bar geometry. In the case of Corbino devices, crosslinked PMMA made by overexposure of the electron-beam resist was used as an insulating bridge between the inner and outer contacts.

To investigate the layer-parity effect, pairs of Corbino devices were fabricated on the same graphite flakes that were chosen to have isolated monatomic steps on the surface. The selection of graphite was based on the optical contrast but the step height was subsequently checked by atomic force microscopy. We then determined the layer parity of the graphite at each side of the step based on the degeneracy period of the fan diagram, which, in combination with measured thickness, allowed us to unambiguously identify the number of layers.

In total, we studied approximately 20 devices in both Hall bar and Corbino geometries with thicknesses ranging from 3.5 to 93 nm. In addition, to distinguish between surface and bulk effects, we fabricated several devices on quartz substrates to carry out capacitance measurements. Furthermore, to check whether stacking faults in graphite destroy the observed 2.5D QHE, we prepared special hBN/graphite-graphite/hBN heterostructures in which the graphite film consisted of two crystals that were intentionally slightly misaligned to form an artificial stacking fault. Such devices exhibited no insulating states essential for observation of the QHE (Supplementary Fig. 9a,b). We also note that hBN encapsulation is crucial for the observation of the 2.5D QHE as witnessed in experiments using similar devices but with graphite placed in direct contact with the rough quartz substrate (no bottom hBN). Its absence ruined the electronic quality of the bottom graphite surfaces, which was sufficient to smear the 2.5D QHE gaps completely (Supplementary Fig. 9d,e). On the other hand, for the properly encapsulated graphite the 2.5D QHE was quite robust and observed in all of our devices, even for lateral sizes up to tens of micrometres (limited only by the maximum area we could find that was free from contamination bubbles) (Supplementary Fig. 9f).

Transport and capacitance measurements. The longitudinal and Hall voltages were recorded using an SR830 lock-in amplifier and applying a.c. currents typically of about 10 nA. Such unusually small currents were found necessary to avoid the suppression of the observed 2.5D QHE (Supplementary Fig. 2). For measurements on the Corbino devices, a small bias (typically 0.1 mV) was applied between the inner and outer contacts, and the current was recorded using again an SR830 amplifier. The capacitance was measured using an on-chip cold bridge based on a high-electron mobility transistor[35]. The typical excitation voltages were in the range from 1 to 10 mV, depending on the thickness of the hBN dielectric layer.

Away from the QHE regime (high temperatures and low magnetic fields), σ_{xx} and σ_{xy} in semimetallic graphite can be described by the expressions $\sigma_{xx}(n_i,\mu_i,B)=\sum_i \frac{n_i e\mu_i}{1+\mu_i^2B^2}$ and $\sigma_{xy}(n_i,\mu_i,B)=\sum_i \frac{n_i e\mu_i^2B}{1+\mu_i^2B^2}$, where n_i and μ_i are the carrier densities and mobilities, respectively, and the index i runs through different types of charge carrier. Using the above expressions, we fitted the measured B and T dependences for σ_{xx} and σ_{xy} and found that the model with just two types of carrier provides good agreement with the experiment. This also allowed us to estimate the charge densities and mobilities in the absence of electrostatic doping (Supplementary Fig. 1).

Tight-binding description of Landau bands in the UQR. The SWMC model[2,8,29] has been widely employed to describe the band structure of graphite. While values of most of the hopping amplitudes (γ_0, γ_1, γ_3 and γ_4) have been well established in the earlier studies, there is no clear consensus about the values of γ_2, γ_5 and a dimer site energy shift Δ; hence, we adjusted them to get the best fitting to the experimental results obtained in the present work. Namely, we chose γ_2, γ_5 and Δ to match the slope of 0, 1 Landau bands dispersion near the Fermi level (which is given by γ_2 with an extra correction coming from γ_3) and the distance δ_{10} between the 0 and 1 Landau bands. Thus, the values of the SWMC parameters we used are $\gamma_0=3.16$ eV, $\gamma_1=0.39$ eV, $\gamma_2=-17$ meV, $\gamma_3=0.315$ eV, $\gamma_4=70$ meV, $\gamma_5=38$ meV and $\Delta=-5$ meV.

The zero-field spectrum of graphite, determined by the SWMC model, contains four bands. Two high-energy bands, $\epsilon_\pm^{\rm split}(k_z,p)$ and

$$\epsilon_\pm^{\rm split}(k_z,p) = \frac{1}{2}(E_\pm+E_3) \pm\sqrt{\frac{1}{4}(E_\pm-E_3)^2+\left(1\mp\frac{\gamma_4\Gamma}{\gamma_0}\right)^2(vp)^2}$$

form a minority hole Fermi surface at the H point ($k_z=\pi/2c$) whereas the other two degenerate low-energy bands, $\epsilon_\pm^{\rm low}(k_z,p)$, which is reminiscent of the bilayer graphene low-energy bands[5], and

$$\epsilon_\pm^{\rm low}(k_z,p) = \frac{1}{2}(E_\mp+E_3) \pm\sqrt{\frac{1}{4}(E_\mp-E_3)^2+\left(1\pm\frac{\gamma_4\Gamma}{\gamma_0}\right)^2(vp)^2}$$

form majority hole and electron Fermi surfaces. Here, $v=\frac{\sqrt{3}\gamma_0 a}{2\hbar}$, $p=\sqrt{p_x^2+p_y^2}$, $E_3=\frac{1}{2}\gamma_2\Gamma^2$, $E_\pm=\Delta\pm\gamma_1\Gamma+\frac{1}{2}\gamma_5\Gamma^2$, $\Gamma=2\cos ck_z$, $a=0.246$ nm, $c=0.335$ nm and $\hbar=h/2\pi$.

In a magnetic field oriented along the z axis, the in-plane momentum $\mathbf{p}$ has to be extended using Kohn–Luttinger substitution, $\mathbf{p}\to-i\hbar\nabla+e\mathbf{A}$, and this leads to the Landau quantization of the lateral motion of electrons and formation of Landau bands[26,34,35]. For $\gamma_3\to0$ there is an analytic expression[2,8,29,36,37] for both valley-degenerate (the symbol $\pm$ below is not affected by the choice of the valley) high-energy ('split') bands

$$\epsilon_\pm^{\rm split}(k_z,m)\approx E_\pm(k_z)+eB\hbar v^2(2m-1)\omega_\pm,$$
$$(m=2,3,\ldots),\omega_\pm=\frac{\left(1\mp\frac{\gamma_4\Gamma}{\gamma_0}\right)^2}{E_\pm(k_z)-E_3(k_z)}$$

and low-energy bands ($m=2, 3, \ldots$)

$$\epsilon_\pm^{\rm low}(k_z,m) \approx E_3(k_z)-eB\hbar v^2 \left[\left(m-\frac{1}{2}\right)(\omega_++\omega_-) \mp\sqrt{\left(m-\frac{1}{2}\right)^2(\omega_+-\omega_-)^2+\omega_+\omega_-}\right]$$

Additionally, the two lowest energy bands ($m=0, 1$) are described by

$$\epsilon_0(k_z)=2\gamma_2\cos^2 ck_z$$

and

$$\epsilon_1(k_z)=2\gamma_2\cos^2 ck_z-eB\hbar v^2(\omega_++\omega_-)$$

for which the wavefunctions are localized at even (odd) layers in +KH (−KH) valleys. In magnetic fields $B>7$ T, the large distance to the higher Landau bands drives graphite into the UQR, leaving only $\epsilon_{0,1}(k_z)$ bands to cross the Fermi level at $k_F\approx\pi/4c$. This yields the 1D Fermi velocity along the z axis, $\hbar v_{Fz}\approx-2\gamma_2 c$ for the electron motion across the film, and the splitting energy between 0 and 1 Landau bands

$$\delta_{10}=\varepsilon_1-\varepsilon_0\approx eB\hbar v^2\left[\frac{\gamma_5+\Delta}{\gamma_1^2}+\frac{4\gamma_4}{\gamma_0\gamma_1}\right]\approx 6.15\mu_B B$$

where $\mu_B=\frac{e\hbar}{2m_e}$ is the Bohr magneton. For the parameters listed above, we estimate $\delta_{10}\approx0.37$ meV T^{-1}, which is about 3 times larger than the single-particle Zeeman energy for electrons in graphite. The Fermi velocity v_{Fz} and the splitting δ_{10} are the parameters that we have matched to the measured gaps and level crossings to fix the above-quoted values of the tight-binding model parameters γ_2, γ_5 and Δ. In Supplementary Fig. 6, we compare the values of δ_{10} to the Zeeman splitting and the standing-wave level spacing in graphite of different thicknesses and layer parities.

Note that the graphite spectrum is not particle–hole symmetric because of the non-zero value of the hopping parameter γ_2. This is seen in Fig. 2a and Supplementary Fig. 3a, where the experimental maps do not exhibit electron–hole symmetry. For instance, the localized surface states of electron–hole asymmetric Landau bands 2^+ and 2^- (see Fig. 2c), which are responsible for the surface

accumulation layers and screening of the gate potential, are reached by the Fermi level and get filled in different B for the same level of n- and p-doping.

Standing waves in the UQR and the layer-parity effect. For our thin graphite devices, it has been found that measurable QHE gaps start to appear in B as low as ~0.5 T (Supplementary Fig. 4). However, for crystals with hundreds of atomic layers, the gaps become sufficiently large, clearly visible and regularly structured only for $B > 7$ T (in the UQR), where only the 0 and 1 Landau bands, $\epsilon_{0,1}$, are left to cross the Fermi level. The spectrum of such films can be described using k_z standing waves within the quasi-1D bands $\epsilon_{0,1}$ and the allowed energies are determined by size quantization of k_z. Electrons in the two Landau bands 0 and 1 form standing waves with the maxima on even graphene layers for the valley +KH and on odd layers for the valley −KH (swapping valleys for $B \to -B$). For a crystal with an even number of layers, $N = 2\mathcal{N}$, there is the same number of even and odd layers to support states in +KH and −KH valleys, which determines the valley-degenerate standing waves with the amplitude $\sin\left(\frac{\pi n j}{\mathcal{N}+1}\right)$ on the jth graphene layer among even or odd sequences. This corresponds to wavenumbers $k_n = \frac{\pi n}{2c(\mathcal{N}+1)}$, where $n = 1 \ldots \mathcal{N}$, and Landau band energies $\epsilon_0(k_n)$ and $\epsilon_1(k_n)$. In graphite with an odd number of layers, $N = 2\mathcal{N}-1$, there are $\mathcal{N}$ odd and $\mathcal{N}-1$ even layers and the standing waves are such that for the valley –KH (on odd layers) $k_n = \frac{\pi n}{2c(\mathcal{N}+1)}$ whereas for the valley +KH (on even layers) $k'_n = \frac{\pi n}{2c\mathcal{N}}$. The difference between standing-wave spectra with even and odd N is illustrated in Fig. 3a and referred to as the layer-parity effect.

Near the Fermi level ($n_F \approx \mathcal{N}/2$) quantized states in each valley form a staircase of levels separated by $\frac{\pi v_F}{2\mathcal{N}c} \approx \frac{\pi |\gamma_2|}{\mathcal{N}}$. For even N, these spectra are valley-degenerate and their spacing is given by $\delta E_{even} \approx \frac{\pi |\gamma_2|}{\mathcal{N}} \approx 94N^{-1}$ meV whereas for odd N, the energy states in the valley +KH are shifted by $\frac{\pi v_F}{4\mathcal{N}c}$ with respect to those in the valley –KH. This lifts the valley degeneracy and, also, reduces the level spacing to $\delta E_{odd} \approx \frac{\pi |\gamma_2|}{2\mathcal{N}} \approx 47N^{-1}$ meV. These energy spacings should be compared to the Landau band splitting given by $\delta_{10} \approx 0.37\,\mathrm{meV\,T^{-1}}$, and the Zeeman splitting, $2\mu_B B$, because altogether they determine the gaps in the quantized spectrum and the hierarchy of 2.5D QHE plateaux.

In the case of even N, valley degeneracy may be broken by an electric field applied in the z direction (Supplementary Fig. 7). However, this effect should disappear in symmetrically gated devices ($n_t = n_b$) due to the recovery of inversion symmetry. For odd-N devices, the symmetric gating would still lead to corrections in the valley splitting, because states in Landau bands 0 and 1 are located on the first and last layer in one valley (and, therefore, are more strongly influenced by gating) whereas states in the other valley are located on the second and penultimate layers and, therefore, are more weakly affected by the same gating. Such corrections can explain a noticeable difference between the measured and simulated fan diagrams for the 35-layer graphite device (Fig. 3b,c) as well as the deviations of the measured gap energies for odd-layer graphite in Fig. 3d from the theoretical curve. In the latter case, for the two blue points that fall onto the red line, the maximal gaps were found at large filling factors. As, for odd N, gate-induced energy shifts of nearby states in different valleys are different, the simple free-particle model is expected to work well only for the first few filling factors where the gate-induced electric field is small. Therefore, notable deviations from the model predictions for these two devices are not surprising.

When we discuss the 2.5D QHE we use the analogy between the Landau level states in bilayer graphene[5] and the states in the lowest two Landau bands in the UQR graphite. That is, we attribute an e^2/h contribution towards σ_{xy} from each filled standing wave (each quantized k_z) of 0 and 1 Landau bands in a given spin and valley state, counting n-type- and p-type-doped filling from the neutrality condition, $n_{tot} = 0$. As a result, σ_{xy} at integer filling factors is exactly proportional to the charge density induced electrostatically in graphite: $\sigma_{xy} = \nu e^2/h = n_{tot} e/B$, in agreement with the case of the conventional QHE.

Surface states. To understand the additional features in the observed Landau fan diagrams (Fig. 2a and Supplementary Fig. 3a), related (as indicated by Fig. 2b and Supplementary Fig. 3b) to the formation of surface states, we appended the SWMC model by the self-consistent analysis of gate-voltage-induced surface charge accumulation, implemented in the Hartree approximation (see ref. [38]). In Supplementary Fig. 3c,d we show examples of numerically stable self-consistent solutions for potential and charge distributions on few surface layers for several values of gate-induced charge carrier densities n_t. For large n_t, one can see in Supplementary Fig. 3c the regions of enhanced compressibility (higher density of states) that correspond to filling localized surface states that split-off from the higher ($m = 2^{\pm}$ and $3^{\pm}$) Landau bands of bulk graphite with electrons trapped in a surface accumulation layer by the self-consistent potential $U(z)$ (Supplementary Fig. 3d). In particular, the 2^+ Landau band forms a surface state for electrons that spawns from the neutrality point at $B \approx 7.5$ T in experimental data (Supplementary Fig. 3a) and at $B \approx 6$ T in theoretical modelling (Supplementary Fig. 3c). Similarly, the localized states chipping off the higher-energy Landau band 3^+ on the n-doping side, and also the Landau band 2^- on the p-doping side, can be identified at smaller B in Supplementary Fig. 3.

Data availability

All relevant data are available from the corresponding authors on reasonable request.

References

33. Mishchenko, A. et al. Twist-controlled resonant tunnelling in graphene/boron nitride/graphene heterostructures. *Nat. Nanotechnol.* **9**, 808–813 (2014).
34. Henni, Y. et al. Rhombohedral multilayer graphene: a magneto-Raman scattering study. *Nano Lett.* **16**, 3710–3716 (2016).
35. Yu, G. L. et al. Hierarchy of Hofstadter states and replica quantum Hall ferromagnetism in graphene superlattices. *Nat. Phys.* **10**, 525–529 (2014).
36. Nakao, K. Landau level structure and magnetic breakthrough in graphite. *J. Phys. Soc. Jpn* **40**, 761–768 (1976).
37. Inoue, M. Landau levels and cyclotron resonance in graphite. *J. Phys. Soc. Jpn* **17**, 808–819 (1962).
38. Koshino, M., Sugisawa, K. & McCann, E. Interaction-induced insulating states in multilayer graphenes. *Phys. Rev. B* **95**, 235311 (2017).